

HUBBLE SPACE TELESCOPE OBSERVATIONS OF THE OLD PULSAR PSR J0108–1431*

VADIM ABRAMKIN,¹ YURIY SHIBANOV,¹ ROBERTO P. MIGNANI,^{2,3} AND GEORGE G. PAVLOV⁴

¹*Ioffe Institute, Politekhmicheskaya 26, St. Petersburg, 194021, Russia*

²*INAF – Istituto di Astrofisica Spaziale e Fisica Cosmica Milano, via E. Bassini 15, I-20133, Milano, Italy*

³*Janusz Gil Institute of Astronomy, University of Zielona Góra, ul Szafrana 2, 65-265, Zielona Góra, Poland*

⁴*The Pennsylvania State University, Department of Astronomy & Astrophysics, 525 Davey Lab., University Park, PA 16802, USA*

ABSTRACT

We present results of optical-UV observations of the 200 Myr old rotation-powered radio pulsar J0108–1431 with the *Hubble Space Telescope*. We found a putative candidate for the far-UV (FUV) pulsar counterpart, with the flux density $f_\nu = 9.0 \pm 3.2$ nJy at $\lambda = 1528$ Å. The pulsar was not detected, however, at longer wavelengths, with 3σ upper limits of 52, 37, and 87 nJy at $\lambda = 4326$, 3355, and 2366 Å, respectively. Assuming that the pulsar counterpart was indeed detected in FUV, and the previously reported marginal *U* and *B* detections with the Very Large Telescope were real, the optical-UV spectrum of the pulsar can be described by a power-law model with a nearly flat f_ν spectrum. Similar to younger pulsars detected in the optical, the slope of the nonthermal spectrum steepens in the X-ray range. The pulsar’s luminosity in the 1500–6000 Å wavelength range, $L \sim 1.2 \times 10^{27} (d/210 \text{ pc})^2$ erg s^{−1}, corresponds to a high efficiency of conversion of pulsar rotation energy loss rate \dot{E} to the optical-UV radiation, $\eta = L/\dot{E} \sim (1-6) \times 10^{-4}$, depending on somewhat uncertain values of distance and spectral slope. The brightness temperature of the bulk neutron star surface does not exceed 59,000 K (3σ upper bound), as seen by a distant observer. If we assume that the FUV flux is dominated by a thermal component, then the surface temperature can be in the range of 27,000–55,000 K, requiring a heating mechanism to operate in old neutron stars.

Keywords: pulsars: individual (PSR J0108–1431) — stars: neutron — ultraviolet: stars

1. INTRODUCTION

Optical and ultraviolet (UV) observations of old rotation-powered pulsars (ages $\gtrsim 1$ Myr), supplemented by X-ray observations, are important to understand advanced stages of thermal evolution of neutron stars (NSs) and study non-thermal emission processes in their magnetospheres. So far, only a handful of such pulsars have been detected in both X-rays and optical-UV. These are the 3 Myr old PSR B1929+10 (Pavlov et al. 1996; Mignani et al. 2002) and the 17 Myr old PSR B0950+08 (Pavlov et al. 1996, 2017), and two a few Gyr old recycled millisecond pulsars, PSR J2124–3358 (Rangelov et al. 2017) and PSR J0437–4715 (Kargaltsev

et al. 2004; Durant et al. 2012), all are identified in the UV-optical with the *Hubble Space Telescope* (*HST*). For both PSR B1929+10 and PSR J2124–3358, the spectral data are insufficient to determine the nature of the optical-UV emission, whereas the others show a Rayleigh-Jeans (R-J) continuum, with an additional power-law (PL) component in PSR B0950+08. In both cases, the inferred temperatures of $\sim 10^5$ K, higher than predicted by NS cooling models (e.g., Yakovlev & Pethick 2004), suggest that some re-heating mechanisms operate in the NS interior. A candidate optical counterpart to the 5 Myr old PSR B1133+16 was found with the Very Large Telescope (VLT), but the identification is still uncertain (Zharikov et al. 2008; Zharikov & Mignani 2013).

Another old pulsar with a yet unconfirmed optical counterpart is PSR J0108–1431. This pulsar was discovered by Tauris et al. (1994) in the Parkes Southern Pulsar Survey (Manchester et al. 1996). Its spin period $P = 0.808$ s and period derivative $\dot{P} = 6.51 \times 10^{-17}$ s s^{−1} (corrected for the Shklovskii effect), imply a rota-

Corresponding author: Vadim Abramkin
vadab94@gmail.com

* Based on observations made with the NASA/ESA *Hubble Space Telescope*, obtained at the Space Telescope Science Institute, which is operated by the Association of Universities for Research in Astronomy, Inc., under NASA contract NAS 5-26555. These observations are associated with program #14249.

tional energy loss rate $\dot{E} = 5.1 \times 10^{30}$ erg s $^{-1}$ and surface magnetic field $B_s = 2.3 \times 10^{11}$ G. With the characteristic age of 196 Myr, PSR J0108–1431 is one of the oldest non-recycled isolated radio pulsars known to date. It lies close to the so-called “graveyard” region in the pulsar P – \dot{P} diagram, and it is among the faintest radio pulsars, with a 400 MHz luminosity of 0.391 mJy kpc 2 for a distance of 210_{-50}^{+90} pc, obtained from the Very Large Baseline Interferometer (VLBI) radio parallax (Deller et al. 2009), corrected for the Lutz-Kelker bias (Verbiest et al. 2012).

In the first deep optical observation of the field of PSR J0108–1431 with the VLT, Mignani et al. (2003) noticed a faint brightness enhancement in the U image within the error ellipse of the Australian Telescope Compact Array (ATCA) radio position, projected near the edge of an elongated background galaxy. However, they concluded that most likely it was not a real detection and reported only upper limits in the V , B and U filters.

The pulsar position measured by the *Chandra X-ray Observatory* by Pavlov et al. (2009) implied a significant proper motion, which, extrapolated to the epoch of the VLT observations, matched the position of the enhancement noticed by Mignani et al. (2003). It prompted Mignani et al. (2008) to propose that the pulsar counterpart had probably been detected with the VLT, with magnitudes $U = 26.4 \pm 0.3$, $B = 27.9 \pm 0.5$, $V > 27.8$. The improved VLBI proper motion, 170.0 ± 1.7 mas yr $^{-1}$ (Deller et al. 2009), made the proposed identification more robust, with a chance positional coincidence probability of $\sim 3 \times 10^{-4}$ (Mignani et al. 2011). The optical spectrum of the PSR J0108–1431 candidate counterpart is poorly defined, although the U and B fluxes are compatible with a $\sim 2.3 \times 10^5$ K R–J spectrum, for the NS radius of 13 km and 210 pc distance.

The PSR J0108–1431 X-ray identification with *Chandra* by Pavlov et al. (2009) has been confirmed by the detection of X-ray pulsations with *XMM-Newton* (Possett et al. 2012). The X-ray spectrum is best fitted by a PL with a (fixed) photon index $\Gamma = 2$ and a blackbody (BB) with temperature $1.28_{-0.12}^{+0.35} \times 10^6$ K and effective radius $R = 43_{-9}^{+16} d_{210}$ m, where d_{210} is the pulsar distance in units of 210 pc, with a hydrogen column density $N_H = 2.3_{-2.2}^{+2.4} \times 10^{20}$ cm $^{-2}$.

The proposed optical identification of PSR J0108–1431, however, has never been confirmed. Follow-up VLT observations in 2009 with about two times larger total exposures were not conclusive because of an almost twice worse seeing of $0''.8 - 1''.0$ (Mignani et al. 2011), as compared to $\approx 0''.5$ in previous observations in 2000 (Mignani et al. 2003). The counterpart was not detected at the expected new position of the pulsar accounting for

its proper motion, while its brightness limits, $U \gtrsim 26.5$, $B \gtrsim 27.2$, were consistent with the tentative detection reported by Mignani et al. (2008). To verify the putative VLT identification, measure the optical-UV spectrum of this pulsar, and constrain the surface temperature of the very old NS, we carried out new observations with the *HST*. We describe the *HST* observations in Section 2 and astrometry of the *HST* images in Section 3. Photometry of the candidate pulsar counterpart in the *HST* and VLT data is reported in Section 4. In Section 5 we discuss spectral fits of the optical-UV data, compare them with the X-ray spectrum, and discuss constraints on the NS surface temperature. Conclusions from our analysis are presented in Section 6.

2. OBSERVATIONS

The PSR J0108–1431 field was observed with the *HST* in 2016 August (program #14249, PI Mignani) using the Ultraviolet-Visible (UVIS) channel of the Wide Field Camera 3 (WFC3; 6 *HST* orbits) and the Solar Blind Channel (SBC) of the Advanced Camera for Surveys (ACS; 2 *HST* orbits). The WFC3/UVIS imaging was carried out with the F438W, F336W and F225W broadband filters, while the F140LP long-pass filter was used with the ACS/SBC. The log of the observations and the pivot wavelengths of the filters are presented in Table 1. For each filter, the total integration time was split into shorter exposures distributed over two *HST* orbits. The WFC3/UVIS exposures were taken in the ACCUM mode, applying a four-point box dither pattern in each orbit. The UVIS2-C1K1C-CTE aperture was used to place the pulsar close to a readout amplifier and minimize the CCD charge transfer efficiency (CTE) losses, as advised in the WFC3 Instrument Handbook¹. The data were reduced and flux-calibrated through the CALWF3 pipeline, which also applies the image de-dithering, geometric distortion and CTE corrections, cosmic-ray filtering, and stacking. For the ACS/SBC, a single exposure was taken in the ACCUM mode during each orbit. The data were processed through the CALACS pipeline including the flux-calibration and geometric distortion correction. The SBC images are not affected by cosmic rays and CTE. The data for two *HST* orbits obtained for each filter (see Table 1) were combined to produce resulting images. However, the aperture door was closed during second ACS/SBC orbit (2900 s) because the Fine Guidance Sensors failed to acquire the guide stars. Since this orbit provided no science data, only the first ACS/SBC orbit is included in Table 1.

¹ See <https://hst-docs.stsci.edu/display/WFC3IHB>.

Table 1. *HST* observations of PSR J0108–1431

Start time ^a	Instrument	Filter	λ_p^b (Å)	$\Delta\lambda^c$ (Å)	Exposure (s)
2016-08-08 15:00:47	WFC3/UVIS	F225W	2359	500	2472
2016-08-08 16:33:47	WFC3/UVIS	F225W	2359	500	2460
2016-08-08 18:09:13	WFC3/UVIS	F336W	3355	550	2580
2016-08-08 19:44:39	WFC3/UVIS	F336W	3355	550	2580
2016-08-08 21:20:04	WFC3/UVIS	F438W	4325	695	2580
2016-08-08 22:55:30	WFC3/UVIS	F438W	4325	695	2580
2016-08-11 22:32:15	ACS/SBC	F140LP	1528	294	2800

NOTE—Each line corresponds to one *HST* orbit.

^a UT start time corresponds to the start of first exposure for the orbit.

^b Pivot wavelength of the filter.

^c Bandwidth (FWHM) of the filter.

Table 2. *Gaia* DR2 positions and p.m. components of the reference objects marked in Figure 1

Object	RA (J2000) ^a	Decl (J2000) ^a	RA-err mas	Decl-err mas	μ_α^b mas yr ⁻¹	μ_δ mas yr ⁻¹
1	01 ^h 08 ^m 09 ^s .001	−14°31′32″.121	0.70	0.55	+0.6 ± 1.9	−5.3 ± 1.2
2	01 ^h 08 ^m 09 ^s .181	−14°32′04″.753	2.0	1.6
3	01 ^h 08 ^m 07 ^s .706	−14°32′01″.488	0.15	0.12	+5.09 ± 0.42	−4.12 ± 0.26
4	01 ^h 08 ^m 15 ^s .742	−14°32′33″.613	0.23	0.18	−6.56 ± 0.65	−30.61 ± 0.41
5	01 ^h 08 ^m 14 ^s .793	−14°32′49″.463	0.30	0.23	+46.72 ± 0.82	−4.43 ± 0.52

^aThe *Gaia* position epoch is 2015.5 (= MJD 57204).

^b μ_α is defined as $\dot{\alpha} \cos \delta$, where α and δ are RA and Decl, respectively.

3. ASTROMETRY

Precise astrometric referencing is crucial for searching the pulsar counterpart by its positional coincidence with the radio pulsar. We used the *Gaia* DR2 Catalog (Lindgren et al. 2018) and the IRAF tasks `imcentroid` and `ccmap` to obtain astrometric solutions. Five catalogued objects fall within the UVIS field of view (FoV) of about $162'' \times 162''$ (pixel scale of 39.6 mas was chosen in drizzling). These objects are best detected in the F438W image which we use as a primary reference image for SBC astrometry (SBC FoV $\approx 31'' \times 34''$; pixel scale 25 mas after drizzling²). The *Gaia* objects are marked and numerated in this image shown in Figure 1; their coordinates and proper motion (p.m.) components μ_α and μ_δ are listed in Table 2. Object 2 looks like an elliptical galaxy and shows no p.m.

We used the coordinates and p.m. values for the four stars in Table 2 to calculate their coordinates at the epoch of the UVIS observations, MJD 57608, for further astrometry. To increase the number of reference objects, we also used the galaxy (object 2). Thanks to its regular (elliptical) shape, the uncertainty of its position in the F438W image is reasonably small, about 2.4 mas. The total (stars plus galaxy) root-mean-square (*rms*) centroid radial uncertainty is 1.9 mas. According to Table 2, the *rms* of the *Gaia* radial uncertainty of the reference objects is 1.3 mas. The p.m. corrections lead to an additional radial uncertainty of 1.3 mas. Performing the astrometric fit with the `ccmap`, we ob-

² For the UVIS and SBC, the original pixel scales are about 40×40 and 31×34 mas, respectively.

tained formal *rms* residuals of 0.7 mas for the right ascension (RA) and 2.3 mas for the declination (Decl). An additional uncertainty of about 2 mas is associated with the WFC3/UVIS geometric distortion correction (Kozhurina-Platais & Anderson 2015). As a result, combining all the uncertainties in quadrature, we got the final radial uncertainty of 4 mas (0.1 pixels) for astrometric referencing of the F438W image.

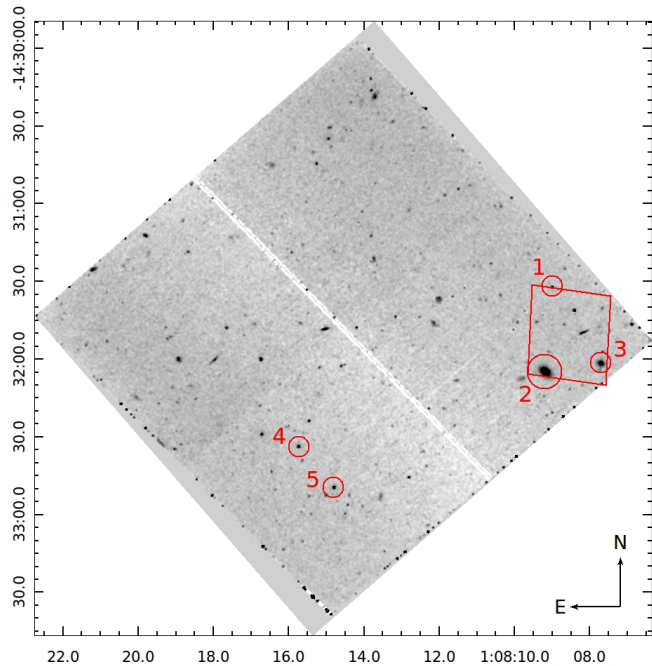


Figure 1. UVIS F438W image of the pulsar field. The image is binned by a factor of 8 (new pixel size is $0''.32$) and smoothed with a 2 pixels Gaussian kernel. Red numbered circles mark the five objects from the *Gaia* DR2 Catalog listed in Table 2 and used for astrometry. The red box shows the SBC FoV presented in Figure 2.

Using the same reference objects for the F336W image yields the net radial astrometric uncertainty of 7 mas. For the F225W image, the *rms* fit residuals are 23 mas for RA and 13 mas for Decl, and the net radial astrometric uncertainty is 49 mas. The degradation of the referencing accuracy, as compared to the F438W image, is caused by a significant brightness decrease of the objects in the images.

An accurate alignment of the F140LP and F438W images is not possible with a standard approach because three of the only four common objects (marked in Figure 2) are extended, with poorly defined positions in the F140LP image. The only common point source is star 3, which, however, becomes much fainter in the F140LP band. We used this star for an initial estimate of the shifts between the F140LP and F438W im-

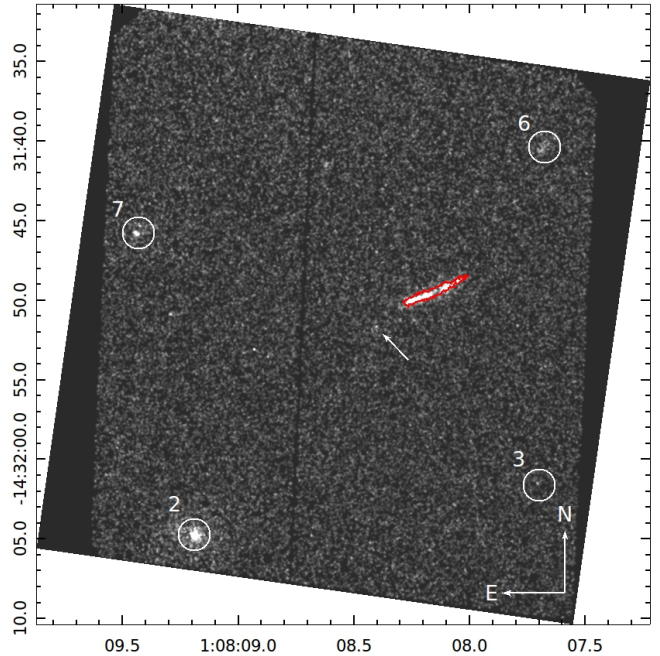


Figure 2. SBC F140LP image of the pulsar field. The image is binned by a factor of 2 (new pixel size $0''.05$) and smoothed with the 3 pixels Gaussian kernel. The arrow shows the pulsar counterpart candidate. White numbered circles mark four objects which, together with a bright spiral galaxy seen edge-on north-west of the candidate, were used to align the SBC image to the UVIS F438W image. Red contours of the spiral galaxy are overlaid from the F438W image to demonstrate robustness of the alignment.

ages, and found offsets of $1''.3$ in R.A. and $0''.4$ in Decl. Their uncertainties are dominated by the position error of ≈ 30 mas of star 3 in the F140LP image. It was conservatively estimated (see, e.g. Neuschaefer & Windhorst 1995) as FWHM of the SBC point spread function (PSF) of $\approx 0''.2$ (Avila & Chiaberge 2016) divided by the signal-to-noise ratio, $S/N \approx 3$, of the star in the image times $\sqrt{8 \ln 2} = 2.35$. The *imcentroid* task yields a similar value. Then we corrected the WCS values in the header of the SBC fits file applying the measured offsets and used the extended objects, particularly the nearby spiral galaxy seen edge-on, that shows a similar structure in both images, to check the shifts and reveal possible signatures of rotation between the two frames. A similar approach was applied by Zharikov et al. (2002) to align the UV and optical frames for PSR B0950+08. Overlaying the frames (see Figure 2), we found no signs of additional shifts or rotation within the uncertainty of $0''.2$ and concluded that the SBC astrometric referencing is confident within this uncertainty.

The most accurate radio position and p.m. of the pulsar were obtained for the reference epoch of MJD 54100

Table 3. Positions of PSR 0108–1431 at different epochs and its p.m. components

Epoch	RA (J2000)	Decl (J2000)	μ_α	μ_δ
MJD			mas yr ⁻¹	mas yr ⁻¹
51752	01 ^h 08 ^m 08 ^s .314(3)	−14°31′49″.207(37)
54100	01 ^h 08 ^m 08 ^s .34702(9)	−14°31′50″.187(1)	+75.1 ± 2.3	−152.5 ± 1.7
57608	01 ^h 08 ^m 08 ^s .3967(15)	−14°31′51″.651(16)
57611	01 ^h 08 ^m 08 ^s .397(7)	−14°31′51″.65(10)

NOTE— The coordinates and proper motions of the radio pulsar in the second line are taken from Deller et al. (2009). They are used to calculate the coordinates at the epochs of the *HST* UVIS and SBC observations (third and fourth lines, respectively) and VLT FORS1 observations (first line). Hereafter, the numbers in brackets are uncertainties related to the last significant digits quoted. The uncertainties in the first, third and fourth lines include the pulsar p.m. propagation errors and the astrometric reference uncertainties of the corresponding images.

with the Very Long Baseline Interferometry observations using the Australian Long Baseline Array (Deller et al. 2009). Using them, we calculated the pulsar coordinates for the epochs of the *HST* and *VLT* observations (Table 3). The uncertainties on the calculated position in the *HST* images (third and fourth lines in Table 3) include the uncertainties of the F438W and F140LP astrometry and the uncertainties due to propagation of the pulsar p.m. errors.

4. POSSIBLE PULSAR COUNTERPART

In the SBC/F140LP image (Figure 2) we found a faint point-like source with coordinates RA = 01^h08^m08^s.403(14) and Decl = −14°31′51″.66(20), consistent with the expected radio pulsar coordinates (see 4th row in Table 3). A zoomed-in region around this source is shown in Figure 3, which clearly demonstrates that the source is located within the circle with the radius of 0′.2 corresponding to the 1 σ uncertainty of the pulsar radio position in this image.

4.1. Photometry of the FUV counterpart candidate

To find an optimal source aperture for the SBC/F140LP photometry of the pulsar counterpart candidate, we calculated the signal-to-noise ratio S/N as a function of radius of circular aperture centered at the brightest source pixel in the unbinned image using the background extracted from the annulus around the same center with inner and outer radii of 20 and 50 pixels (area $A_b = 4.12$ arcsec²). We found the maximum S/N = 2.7 in the aperture of 8 pixels (0′.2) radius (area $A_s = 0.126$ arcsec²). This aperture was selected as the optimal one. According to Table 2 in Avila & Chiaberge (2016), it contains the fraction $\phi_E \approx 0.63$ of the total number of point source counts.

Following Guillot et al. (2019), we estimated the mean background \bar{C}_{bgd} and its standard deviation σ_{bgd} for a

set of 1000 circular background regions of size $r_{\text{extr}}=0′.2$ (8 pixels, the same as of the source aperture), randomly placed in the annulus. To convert the count rate to the flux density, we took into account the recent correction of the SBC sensitivity, such that the flux density at a given count rate is about 0.77 of the previously adopted value (Avila et al. 2019). The results are presented in Table 4.

As the putative pulsar counterpart is detected at only about 3 σ level, we cannot rule out that the count rate

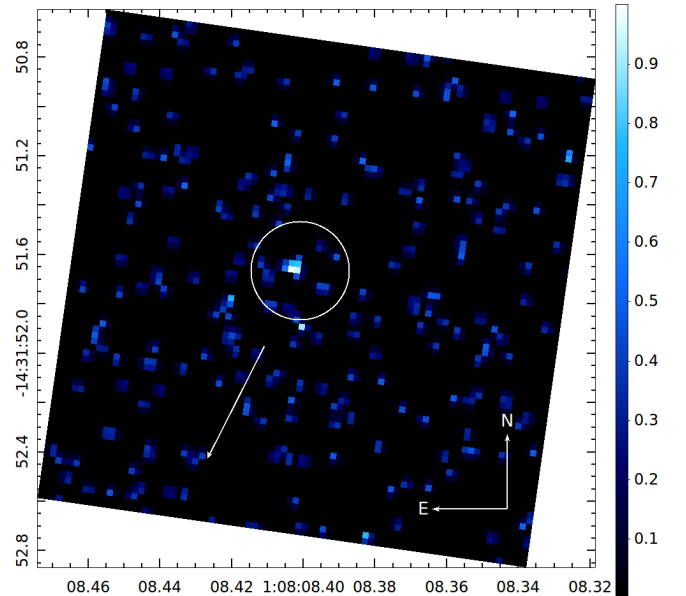


Figure 3. 2'' \times 2'' region of the unbinned and unsmoothed SBC F140LP image around the pulsar. The color bar decodes the image intensity in counts per pixel. The 0′.2 radius circle and the arrow mark the 1 σ radio pulsar position uncertainty and the direction of its p.m. A faint point-like counterpart candidate to the pulsar is clearly visible within the circle.

Table 4. SBC photometry of the pulsar counterpart candidate

N_t	C_{pos}	$\overline{C}_{\text{bgd}}$	σ_{bgd}	N_s	C_s	f_ν
(cts)	(cts/ks)	(cts/ks)	(cts/ks)	(cts)	(cts/ks)	(nJy)
15.3	5.5	2.0	0.7	9.8 ± 3.7	5.6 ± 2.0	9.0 ± 3.2

NOTE— N_t is the total number of counts in the $A_s = 0.126$ arcsec² source aperture, $C_{\text{pos}} = N_t/t_{\text{exp}}$ is the count rate measured in the source aperture ($t_{\text{exp}} = 2.8$ ks is the exposure time), $\overline{C}_{\text{bgd}}$ and σ_{bgd} are the mean and standard deviation of background measurements in 1000 circles with the $0''.2$ radius in the $A_b = 4.12$ arcsec² annulus, N_s is the net source count number in the source aperture, its error is estimated as $[(\sigma_{\text{bgd}}t_{\text{exp}})^2 + N_s]^{1/2}$, $C_s = N_s/t_{\text{exp}}/\phi_E$ is the aperture-corrected net source count rate, $\phi_E \approx 0.63$ (Avila & Chiaberge 2016) is a fraction of source counts in the $r = 0''.2$ aperture, $f_\nu = C_s\mathcal{P}_\nu$ is the flux density at the pivot wavelength $\lambda_{\text{piv}} = 1528$ Å, and $\mathcal{P}_\nu = 1.61$ nJy ks cts⁻¹ is the count-rate-to-flux conversion factor.

excess at the pulsar position is caused by some fluctuation. In this case, one can estimate the flux density upper bound following Kashyap et al. (2010) and Guillot et al. (2019). We define the upper bounds C_{ub} on the pulsar count rate as $C_{\text{ub}} = C_{\text{pos}} - \overline{C}_{\text{bgd}} + n\sigma_{\text{bgd}}$, where C_{pos} is the measured count rate at the position of the pulsar, $\overline{C}_{\text{bgd}}$ and σ_{bgd} are defined above (see also Table 4), and n determines the significance level of the upper bound³. The resulting 3σ upper bounds are $C_{\text{ub}} = 5.5$ cts/ks and $f_\nu^{\text{ub}} = 14$ nJy.

4.2. UVIS upper bounds and VLT observations of PSR J0108-1431

The counterpart candidate is not detected in the UVIS images. Therefore, we calculated the upper bounds on the pulsar count rate and flux density for each of the UVIS filters using the same approach as for the F140LP filter. The sizes of the extraction regions used to measure C_{pos} were chosen by identifying in each image the extraction radius that maximizes S/N for a point source (star). For each of the filters, we estimated $\overline{C}_{\text{bgd}}$ and σ_{bgd} from a set of 1000 circular background regions of size r_{extr} , randomly selected in the annulus of 10 pixels and 30 pixels inner and outer radii around the pulsar position. These quantities, together with C_{ub} and the corresponding flux densities corrected for the finite extraction aperture, $f_\nu^{\text{ub}} = C_{\text{ub}}\mathcal{P}_\nu\phi_E^{-1}$, are presented in Table 5 where we also show the 1σ flux density upper bounds used in spectral fits (Section 5.2).

We also do not detect any object in any of the *HST* bands at the position where Mignani et al. (2008) found a possible pulsar counterpart in the VLT *U* and *B* bands near the northern edge of the spiral galaxy. For the *HST*-VLT consistency check, we re-reduced the VLT *UBV* data using the recent version of the ESO recipe

execution tool EsoRex 3.13.12⁴. To maximize the spatial resolution and better resolve the putative counterpart from the galaxy, we selected six best-seeing 900 s exposures of eight available in *B*, three 1800 s exposures of five available in *U*, and all twelve 600 s exposures in *V*⁵. This resulted in an extremely good seeing on the stacked images of $0''.56$ in the *U* and *B* bands and $0''.54$ in the *V* band.

The VLT astrometric solution was also revised using 11 relatively bright unsaturated *Gaia* stars, with account for their p.m. shifts for the epoch of the VLT observations. This resulted in a 30 mas uncertainty of the WCS referencing of all images in both coordinates, which is significantly better than the previous astrometric precision of 190 mas based on the GSC-II catalog (Mignani et al. 2008). The more precise astrometry supports the assumption that the object detected with the VLT at a 2σ significance in the *U* and *B* bands is the counterpart candidate. Stacking the *U* and *B* images increases the detection significance to 3σ . The region of this image containing the pulsar is shown in the left panel of Figure 4. For comparison, we also merged the *HST*/UVIS images in the F336W and F438W bands. The respective region is presented in the right panel of Figure 4. Not only the VLT source proposed as the pulsar counterpart is not seen in the F336W+F438W image but also some other faint VLT objects, such as sources 3 and 8–11 in Mignani et al. (2003), are also either resolved only marginally or not visible. At the same time, bright structures of the spiral galaxy are better resolved with the *HST*.

Photometric calibration of the VLT data was carried out using Landolt’s standards PG1323–086, PG0231+051 and PG2331+055, observed at the same nights as the target; it resulted in the following magnitude zero-

³ This definition of C_{ub} is applicable at $C_{\text{pos}} \geq \overline{C}_{\text{bgd}}$, which is fulfilled in our case.

⁴ <https://www.eso.org/sci/software/cpl/esorex.html>

⁵ For the VLT observation log, see Mignani et al. (2003).

Table 5. Upper bounds on count rates and mean flux densities in the UVIS filters at the pulsar radio position, $\alpha=01^{\text{h}}08^{\text{m}}08^{\text{s}}.397$ and $\delta=-14^{\circ}31'51''.65$, at the *HST* observations epoch (MJD 57608)

Filter	λ_{piv} (Å)	t_{exp} (s)	r_{extr} ($''$)	ϕ_E (%)	C_{pos} (cts/ks)	$\overline{C}_{\text{bgd}} \pm \sigma_{\text{bgd}}$ (cts/ks)	C_{ub} (cts/ks)	\mathcal{P}_ν (nJy ks/cts)	$f_{\nu,3\sigma}^{\text{ub}}$ (nJy)	$f_{\nu,1\sigma}^{\text{ub}}$ (nJy)
F438W	4326	5160	0.14	81	47	16 ± 24	102	0.416	52	28
F336W	3355	5160	0.12	78	27	13 ± 16	61	0.470	37	20
F225W	2366	4932	0.14	74	46	16 ± 17	82	0.783	87	50

NOTE— C_{ub} and $f_{\nu,3\sigma}^{\text{ub}}$ are the 3σ upper bounds; $f_{\nu,1\sigma}^{\text{ub}}$ is the 1σ upper bound.

Table 6. 3σ upper bounds on count rate and mean flux density at the pulsar radio position, $\alpha=01^{\text{h}}08^{\text{m}}08^{\text{s}}.314$ and $\delta=-14^{\circ}31'49''.207$, at the VLT observations epoch (MJD 51752)

Filter	λ (Å)	t_{exp} (s)	r_{extr} ($''$)	ϕ_E (%)	C_{pos} (cts/ks)	$\overline{C}_{\text{bgd}} \pm \sigma_{\text{bgd}}$ (cts/ks)	C_{ub} (cts/ks)	\mathcal{P}_ν (nJy ks/cts)	$f_{\nu,3\sigma}^{\text{ub}}$ (nJy)
F438W	4326	5160	0.14	81	13	15 ± 17	50	0.416	26
F336W	3355	5160	0.12	78	6.4	12 ± 13	40	0.470	24
F225W	2366	4932	0.14	74	25	6 ± 13	59	0.783	62
F140LP	1528	2800	0.2	63	0.9	2.1 ± 0.6	1.8	1.61	5

NOTE—For the F438W, F336W and F140LP bands, $C_{\text{pos}} < \overline{C}_{\text{bgd}}$ and the upper bounds are calculated as $C_{\text{ub}} = 3\sigma_{\text{bgd}}$.

points for the stacked images: $Z_U = 25.08 \pm 0.04$, $Z_B = 27.55 \pm 0.05$ and $Z_V = 28.00 \pm 0.01$, calculated for the fluxes in units of the CCD electron rate. For photometry of the putative pulsar counterpart, we used apertures of 2.5 pixel in *U* and 1.3 pixel in *B* (the pixel scale was $0''.2$) which correspond to the enclosed energy fraction of 0.67 and 0.3, respectively, measured using bright unsaturated stars. Such small apertures were used because of proximity of the bright spiral galaxy leading to large systematic errors. We obtained flux densities of the source of 44 ± 22 nJy and 30 ± 14 nJy in the *U* and *B* bands, respectively, and a 3σ upper bound of 36 nJy in the *V* band. The fluxes are consistent, within the uncertainties, with the results obtained by Mignani et al. (2008).

To understand the nature of the putative VLT pulsar counterpart, we calculated the *HST* upper bounds at its position in the VLT observations epoch (Table 6). The derived flux density 3σ upper bounds of 24 nJy in the F336W band and 26 nJy in the F438W band are somewhat lower than the flux densities in the VLT *U* and *B* bands, respectively, presented above. This implies that the VLT object has disappeared or moved out of its place by the epoch of the *HST* observations, i.e., it is not a steady field object. On the other hand,

our 3σ upper bounds of 37 nJy in the F336W band and 52 nJy in the F438W band at the pulsar position at the *HST* epoch (Table 5) are comparable to the *U* and *B* band flux densities⁶. This suggests that the faint pulsar counterpart was indeed seen in the *U*, *B* and F140LP bands, and it could be seen in the *HST* F336W and F438W bands if the exposures were just a factor of 1.5 longer.

Thus, we cannot rule out the possibility that both the VLT (*U* and *B* bands) and *HST* (F140LP band) detected the pulsar counterpart, but further deep observations are needed to prove it.

5. DISCUSSION

We likely detected the putative pulsar FUV counterpart in the F140LP band. Our photometric measurements show that its brightness is near the SBC detection threshold for the one-orbit *HST* observation. Three *HST* orbits would be needed to confirm the FUV counterpart at a 5σ significance. Nevertheless, the tentative detections with the *HST* ACS/SBC and VLT FORS1 *U*, *B* bands, combined with the upper bounds obtained

⁶ Difference of the upper bounds at the two pulsar positions is due to different properties of the local backgrounds.

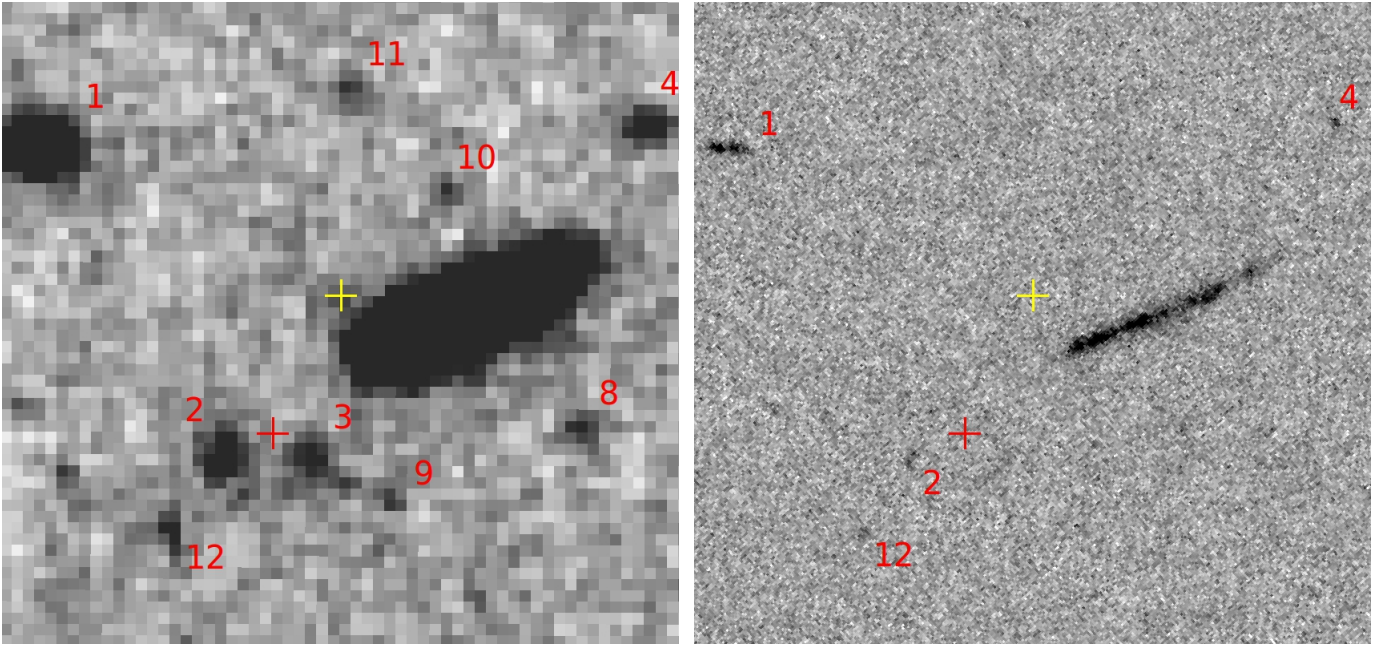


Figure 4. $12''0 \times 11''5$ vicinity of the pulsar as seen with the VLT in the $U+B$ band (*left:*) and with the *HST*/UVIS in the $F438W+F336W$ band (*right:*). North is up and east is left. Smoothing with the Gaussian kernel radius of 1 pixel is applied to the VLT image. The sources are numerated using the nomenclature of Mignani et al. (2003). Pulsar radio positions at the VLT epoch (2000) and the *HST* epoch (2016) are shown by yellow and red crosses, respectively. A faint source is marginally detected in the VLT image near the 2000 position of the pulsar, while it is absent in the *HST* image (for details see Sect. 4.2)

in the UVIS (and VLT V) bands, as well as the *Chandra* and *XMM-Newton* X-ray data, can provide interesting constraints on the optical-UV-X-ray spectral energy distribution (SED) of this old pulsar.

5.1. Extinction towards PSR J0108-1431

According to the Galactic 3D extinction map by Green et al. (2018), the color excess $E(B - V)$ varies between 0.00 and 0.04 within the uncertainty of the distance to the pulsar, and $E(B - V) = 0.02^{+0.02}_{-0.01}$ for $d = 210$ pc.

The $E(B - V)$ value is correlated with the effective hydrogen column density N_{H} for X-ray photoelectric absorption models. Applying the empirical relation $N_{\text{H}} = (0.7 \pm 0.1) \times 10^{22} E(B - V) \text{ cm}^{-2}$, obtained by Watson (2011) for the Galaxy using observations of X-ray afterglows of a large number of γ -ray bursts, we expect $N_{\text{H}} = 1.4^{+1.8}_{-0.8} \times 10^{20} \text{ cm}^{-2}$.

Alternatively, N_{H} can be estimated using the pulsar's dispersion measure, $\text{DM} = 2.38 \text{ pc cm}^{-3}$ and the correlation between DM and N_{H} obtained by He et al. (2013), $N_{\text{H}} = 0.30^{+0.13}_{-0.09} \times 10^{20} \text{ DM cm}^{-2}$, which yields $N_{\text{H}} = 0.71^{+0.31}_{-0.21} \times 10^{20} \text{ cm}^{-2}$, in agreement with the value derived from $E(B - V)$. This also overlaps with the N_{H} range of $(0.3 - 0.8) \times 10^{20} \text{ cm}^{-2}$ at $d = 210$ pc obtained from the study of interstellar NaD absorption lines (Posselt et al. 2007, 2008).

Finally, the phase-integrated X-ray spectrum of the pulsar obtained with *XMM-Newton* is most plausibly

described by the absorbed power law (PL) plus blackbody (BB) model with $N_{\text{H}} = 2.3^{+2.4}_{-2.3} \times 10^{20} \text{ cm}^{-2}$ (Posselt et al. 2012; Arumugasamy & Mitra 2019). The latter value is very uncertain but consistent with the above estimates.

All in all, we can accept $E(B - V) = 0.01-0.03$ as the most probable color excess range for de-reddening of the optical-UV data and combining them consistently with the X-ray data. Using this color excess range and the extinction law from Cardelli et al. (1989), we can calculate the extinction A_{λ} , and the de-reddened source flux density or its upper bound for all the bands where the pulsar was observed. These quantities are presented in Table 7 and Figure 5.

5.2. Multi-wavelength spectrum of PSR J0108-1431

Optical-UV emission from a rotation powered pulsar generally consists of two components, thermal and non-thermal. The nonthermal component, produced by relativistic particles in the pulsar magnetosphere, is usually described by a power-law (PL) model, $f_{\nu} \propto \nu^{\alpha}$, while the spectrum of the thermal component, emitted from the NS surface, is close to a blackbody spectrum (Mignani 2011). In middle-aged (0.1–1 Myr) and moderately old (1–10 Myr) pulsars the nonthermal component dominates in the optical while the thermal component dominates in FUV (e.g., Koptsevich et al. 2001; Zharikov et al. 2004; Shibanov et al. 2006; Kargaltsev & Pavlov

Table 7. De-reddened flux densities and $3\sigma(1\sigma)$ flux density bounds of the pulsar counterpart (in nJy), and PL fit parameters, for three values of $E(B - V)$.

$E(B - V)$	f_U	f_B	f_V	f_{F140LP}	f_{F225W}	f_{F336W}	f_{F438W}	α	f_0
0.01	46 ± 23	31 ± 14	$< 37(26)$	9.7 ± 3.4	$< 94(54)$	$< 39(21)$	$< 54(29)$	$-0.71^{+0.74}_{-0.41}$	$16.2^{+3.3}_{-7.1}$
0.02	48 ± 24	33 ± 16	$< 38(27)$	10.5 ± 3.7	$< 101(58)$	$< 41(22)$	$< 56(30)$	$-0.63^{+0.81}_{-0.45}$	$16.7^{+3.5}_{-7.8}$
0.03	50 ± 25	34 ± 16	$< 39(27)$	11.3 ± 4.0	$< 109(63)$	$< 43(23)$	$< 58(31)$	$-0.60^{+0.77}_{-0.44}$	$17.7^{+3.6}_{-8.2}$

NOTE— Extinction values A_λ , used for de-reddening, were calculated using the extinction law from Cardelli et al. (1989). HST upper bounds were calculated at the pulsar radio position, $\alpha=01^{\text{h}}08^{\text{m}}08^{\text{s}}.397$ and $\delta=-14^{\circ}31'51''.65$, at the HST observations epoch (MJD 57608).

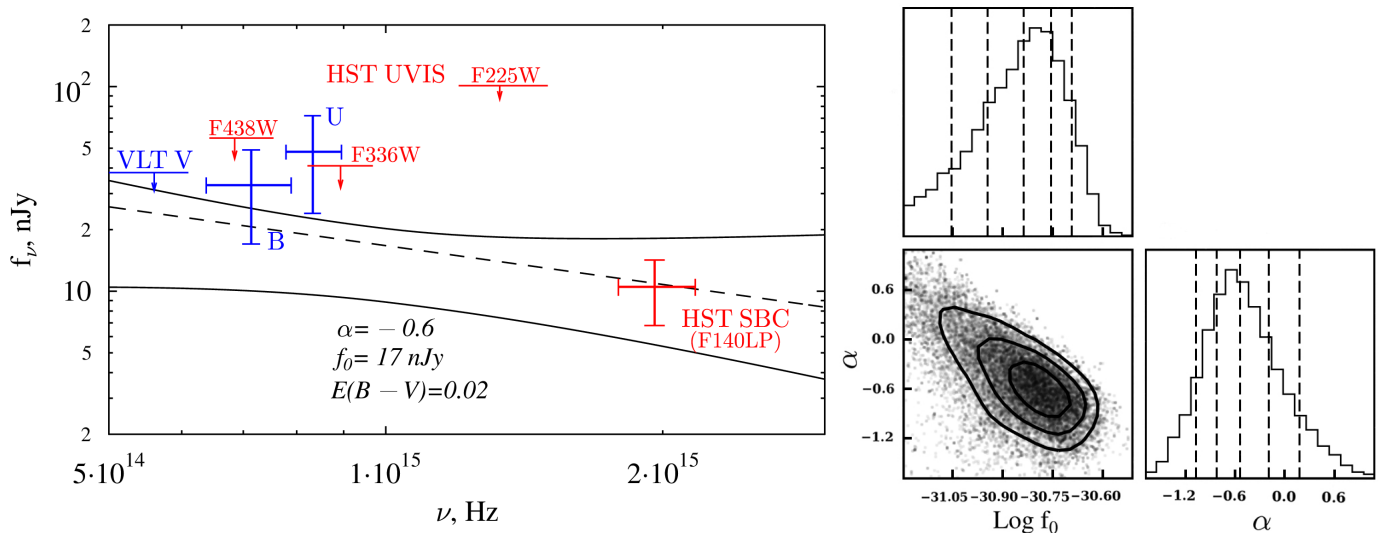


Figure 5. *Left:* Unabsorbed optical-UV SED of the pulsar counterpart candidate for $E(B - V) = 0.02$. Red and blue error bars and downward arrows show flux densities and 3σ upper bounds measured with the HST and VLT, respectively, with instruments and filters indicated in the plot. The dashed and solid lines correspond to the best fit of the data by the PL model and its 90% credible uncertainty, respectively. *Right:* 2D and 1D marginal posterior probability distributions for the PL model parameters $\log f_0$ and α (f_0 in units of $\text{erg cm}^{-2} \text{s}^{-1} \text{Hz}^{-1}$). Vertical dashed lines in the 1D plots correspond to the 10%, 25%, 50%, 75%, and 90% percentiles of the distributions. The contours in the 2D plot represent the levels at 75%, 50%, and 25% of the maximum probability value.

2007; Pavlov et al. 2017), However, we know too little about optical-UV emissions of pulsars as old as PSR J0108–1431; the only other very old pulsar, J2144–3933 with the age of 300 Myr, observed in the optical-UV, was not detected (Guillot et al. 2019). Therefore, we should explore various options and their connection with the results in X-rays where spectra of very old pulsars, including PSR J0108–1431, typically show only the PL component of the NS magnetosphere origin and a thermal component from small hot spots at the NS surface near magnetic pole regions heated by relativistic particles generated in its magnetosphere.

5.2.1. Possible power-law spectrum of the tentative pulsar counterpart

Assuming both optical (B and U) and FUV (F140LP) detections were real, we can fit the unabsorbed flux density points with a PL model: $f_\nu = f_0(\nu/\nu_0)^\alpha$, where we choose the reference frequency $\nu_0 = 1 \times 10^{15}$ Hz. Following the approach suggested by Sawicki (2012) and developed by Drouart & Falkendal (2018), in addition to the three detected SED data points, we also included in the fits the four non-detections (1σ upper bounds) in other filters presented in Table 7. Specifically, we used the Python package Mr-Moose (Drouart & Falkendal 2018), which allows data fitting in a Bayesian framework implementing the Markov chain Monte Carlo (MCMC) approach. To do that, we included FWHM of the HST and VLT filters into the `filters` directory of the Mr-Moose distributive. For the MCMC convergence, we utilized

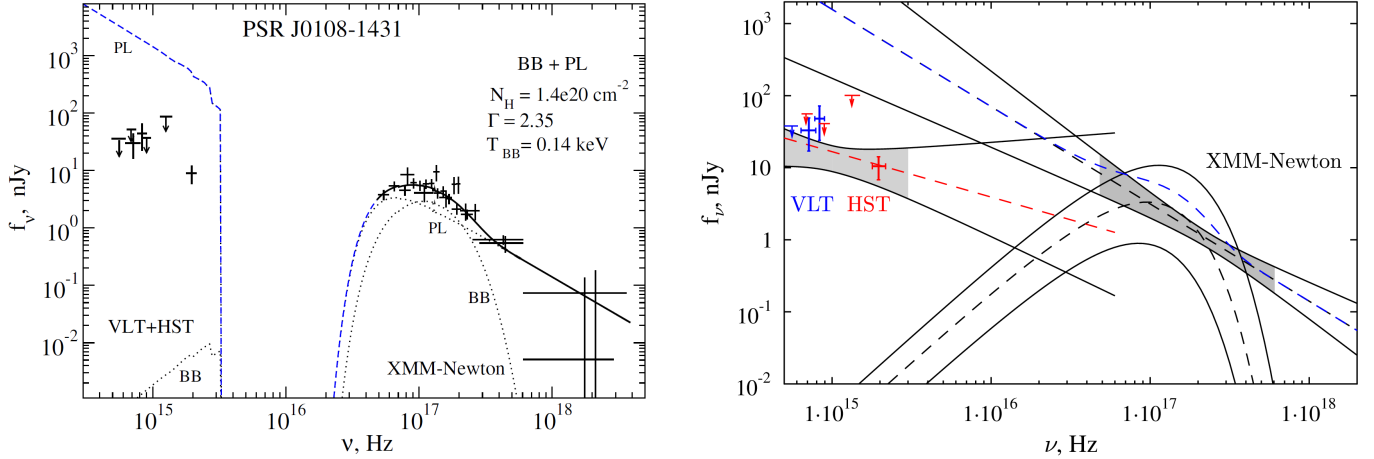


Figure 6. Absorbed (left panel) and unabsorbed (right panel) multiwavelength spectra of the pulsar. The *XMM-Newton* X-ray spectrum is described by a combination of a PL component with a photon index $\Gamma = 2.35^{+0.35}_{-0.40}$ plus a BB component with a temperature $kT = 0.14^{+0.03}_{-0.02}$ keV, at a fixed hydrogen column density $N_H = 1.4 \times 10^{20} \text{ cm}^{-2}$. The dashed blue line in the left panel shows an extrapolation of the best-fit model spectrum to the optical-UV range, which strongly overshoots the observed optical-UV data points shown in this plot. The red line in the right panel shows the best PL fit with $\alpha = -0.6$ to the optical-UV data points dereddened with $E(B - V) = 0.02$, while black lines correspond to the 10% and 90% percentiles of the probability distribution of the optical-UV fit parameters. Blue dashed line shows the best-fit X-ray model spectrum, whereas black lines show its components and their uncertainties.

1000 walkers and 1000 steps. The fitting parameters were the spectral index α and the PL normalization f_0 , which were allowed to vary in wide ranges between -1.7 and 1.1 for α and between -31.2 and -30.5 for $\log f_0$ (where f_0 in units of $\text{erg cm}^{-2} \text{ s}^{-1} \text{ Hz}^{-1}$). Their best-fit values with uncertainties, corresponding to 10 and 90 percentiles of the parameter distribution obtained by cumulative integration of the posterior probability density function, are presented in Table 7. Large uncertainties in the data result in large uncertainties of the PL parameters, and the parameter ranges are almost insensitive to $E(B - V)$. As an example, we show the fit results for $E(B - V) = 0.02$ in Figure 5, where the right panel shows 1D and 2D marginalized posterior probability distributions of the parameters reflecting the fit convergence and quality. The fit results practically do not depend on the *HST*/*UVIS* flux upper bounds, while they are critically affected by the *VLT* upper bound in the *V* band. We also tried to include into the fit the *VLT* *U* and *B* band upper bounds of 2009, which are consistent with the detections in these bands of 2000 (see Sec. 1). This led to a marginal flattening of the best-fit PL. For instance, we obtained $\alpha \approx -0.57$ instead of -0.63 without these upper bounds, for $E(B - V) = 0.02$. Such a small difference is insignificant accounting for the large error budget (see Table 7).

The obtained constraints on the spectral index of the pulsar’s nonthermal emission are compatible with (broader than) a typical range $-0.7 \lesssim \alpha \lesssim 0.2$ for other pulsars observed in the optical-UV range

(e.g., Mignani 2011; Mignani et al. 2019). The best-fit PL parameters correspond to the optical-UV flux $F(1500 - 6000 \text{ \AA}) = 2.3 \times 10^{-16} \text{ erg cm}^{-2} \text{ s}^{-1}$ and luminosity $L(1500 - 6000 \text{ \AA}) = 1.2 \times 10^{27} d_{210 \text{ pc}}^2 \text{ erg s}^{-1}$. Comparing the latter value with the FUV luminosities of pulsars that have been detected in this range (Mignani et al. 2019), we see that J0108-1431 might be the least luminous FUV pulsar. On the other hand, the efficiency of conversion of pulsar rotation energy to optical-UV radiation is $\eta_{\text{opt-UV}} = L(1500 - 6000 \text{ \AA})/\dot{E} = 2.4 \times 10^{-4} d_{210 \text{ pc}}^2$. Accounting for the distance and fit uncertainties, the efficiency could be anywhere in the range $0.7 \lesssim \eta_{\text{opt-UV}}/10^{-4} \lesssim 5.9$. Even for lower values from this range, PSR J0108-1431 is the most efficient nonthermal emitter among pulsars detected in the optical-UV. For instance, based on the data obtained by Pavlov et al. (2017), the 17 Myr old PSR B0950+08 shows about two orders of magnitude lower $\eta_{\text{opt-UV}}$ of about 6×10^{-6} in the same range. A typical optical efficiency range of pulsars is $10^{-7} - 10^{-5}$, only the very young and much more energetic Crab and B0540-69 pulsars have efficiencies comparable to the above estimate for J0108-1431 (Zharikov et al. 2006; Mignani et al. 2010; Kirichenko et al. 2015).

On the other hand, the pulsar is also a highly efficient nonthermal emitter in X-rays with $\eta_X \sim 0.003 - 0.006$ (Posselt et al. 2012). This results in the ratio of the nonthermal optical-UV to the X-ray luminosity $L(1500 - 6000 \text{ \AA})/L_X \sim 0.02 - 0.04$, marginally compatible with a typical range of $0.001 - 0.01$ for pulsars ob-

served in the optical-UV and X-rays (Zavlin & Pavlov 2004; Zharikov et al. 2006).

It is interesting to compare the optical-UV spectrum of the pulsar candidate with the X-ray spectrum of PSR J0108–1431 obtained with *XMM-Newton* (Posselt et al. 2012; Arumugasamy & Mitra 2019). The latter presumably consists of a magnetospheric PL component and a thermal component emitted from hot polar caps. Using the XSPEC tool (ver. 12.11.0)⁷, we fit the time-integrated spectra obtained by *XMM-Newton* EPIC-pn and MOS1 instruments in the 0.2–10 keV range with the absorbed PL+BB model at fixed $N_H = 1.4 \times 10^{20} \text{ cm}^{-2}$, corresponding to $E(B - V) = 0.02$. We obtained the photon index $\Gamma = 2.35^{+0.35}_{-0.40}$ (i.e., $\alpha_X = -\Gamma + 1 = -1.35^{+0.35}_{-0.40}$), the PL normalization $(1.4 \pm 0.4) \times 10^{-6} \text{ ph cm}^{-2} \text{ s}^{-1} \text{ keV}^{-1}$ at $E = 1 \text{ keV}$, the temperature $kT_{\text{BB}} = 0.14^{+0.03}_{-0.02} \text{ keV}$ ($T_{\text{BB}} = 1.6^{+0.3}_{-0.2} \text{ MK}$), and the BB radius $R_{\text{BB}} = 22^{+23}_{-18} d_{210} \text{ m}$ ($\chi^2_\nu \approx 0.9$ for $\nu = 20$ d.o.f). The fit parameters are consistent, within the uncertainties (quoted above at a 1σ confidence level), with those obtained by Posselt et al. (2012), who fixed photon index (at $\Gamma = 2.0$) instead of N_H . The obtained temperature is within the range of typical BB temperatures of hot polar caps of old pulsars, while the BB radius is a factor of 10 smaller than the “canonical” cap radius $R_{\text{pc}} = R_{\text{NS}}(2\pi R_{\text{NS}}/cP)^{1/2} \approx 238 \text{ m}$ for $P = 0.808 \text{ s}$, assuming a plausible intrinsic NS radius $R_{\text{NS}} = 13 \text{ km}$. A similar discrepancy between R_{BB} and R_{pc} is observed in other old pulsars (see Sznajder & Geppert 2020; Posselt et al. 2012, and references therein). Figure 6 shows the fit, for the absorbed and unabsorbed spectra, together with the PL fit to the optical-UV spectrum shown in Figure 5. We see that the continuation of the X-ray model spectrum dominated by the PL component into the optical-UV lies well above the optical-UV detections and upper limits. If we associate the optical-UV and X-ray PL components with the pulsar’s magnetosphere emission, we can conclude that its spectrum steepens with increasing photon energy towards X-rays and has a spectral break somewhere between the UV and soft X-rays, similar to other (younger) pulsars that were detected in both X-rays and the optical (e.g., Karagtsev & Pavlov 2007). However, better quality data in both ranges are needed to make a convincing multi-wavelength spectral analysis.

Based on the high optical through X-ray efficiency of J0108–1431, one can speculate that for old pulsars the highest efficiency range migrates from γ -rays towards lower photon energies.

⁷ See <https://heasarc.gsfc.nasa.gov/docs/xanadu/xspec>

5.2.2. Possibility of thermal emission in FUV and limits on surface temperature

The main goal of these observations was to constrain the NS surface temperature. First of all, we note that if the optical emission allegedly detected with the VLT were thermal, then the FUV flux should be much higher than either its presumably measured value or the upper bound, at any reasonable temperature and size of the emitting NS surface. Therefore, we can rule out the temperature estimate by Mignani et al. (2008) derived from the assumption that the optical spectrum is a Rayleigh-Jeans part of thermal emission from the entire NS surface.

On the other hand, it is possible that the FUV emission is due, at least partly, to a thermal component. If the U and B detections are associated with the pulsar, then the relatively low upper limit on the V flux does not allow a steep negative slope of the PL component, which leaves little room for the thermal component in F140LP. If, however, the U and B detections are not associated with the pulsar while the F140LP detection is, then the F140LP flux could be entirely thermal. As seen from Figure 6, it cannot come from hot polar caps of the pulsar seen in X-rays, but can only come from a cooler bulk surface of the NS. Assuming that the spectrum of the NS surface emission is described by the Planck function, $B_\nu(T) = (2h\nu^3/c^2)[\exp(h\nu/kT) - 1]^{-1}$, its brightness temperature can be estimated from the observed flux density,

$$f_\nu = (R_\infty/d)^2 \pi B_\nu(T_\infty) 10^{-0.4A_\nu}, \quad (1)$$

where $T_\infty = T/(1+z)$ K and $R_\infty = R(1+z)$ km are the NS temperature and radius as measured by a distant observer, $z = [1 - 2.953(M/M_\odot)(1 \text{ km}/R)]^{-1/2} - 1$ is the gravitational redshift. For the F140LP filter ($\nu_{\text{piv}} = 1.96 \times 10^{15} \text{ Hz}$, $A_\nu = 8.15E(B - V)$), we have

$$T_\infty = \frac{9.42 \times 10^4 \text{ K}}{\ln \left[1 + \frac{187 \text{ nJy}}{f_{\text{F140LP}}} \left(\frac{R_{15}}{d_{210}} \right)^2 10^{-3.26E(B-V)} \right]}, \quad (2)$$

where $R_{15} = R_\infty/15 \text{ km}$, and $d_{210} = d/210 \text{ pc}$.

For plausible $d = 210 \text{ pc}$, $E(B - V) = 0.02$, and $R_\infty = 15.8 \text{ km}$ (which correspond to $R = 13 \text{ km}$ at $M = 1.4M_\odot$), the measured FUV flux density $f_{\text{F140LP}} = 9.0 \pm 3.2 \text{ nJy}$ yields $T_\infty = 3.1^{+0.3}_{-0.4} \times 10^4 \text{ K}$ ($T = 3.8^{+0.3}_{-0.5} \times 10^4 \text{ K}$). The optical-UV part of this thermal spectrum with its uncertainties is shown in the left panel of Figure 7. In the right panel of this figure, we show the dereddened thermal spectrum at an upper end of plausible distances, $d = 300 \text{ pc}$, and a lower end of plausible radii, $R_\infty = 13.1 \text{ km}$ (corresponding to $R = 10$

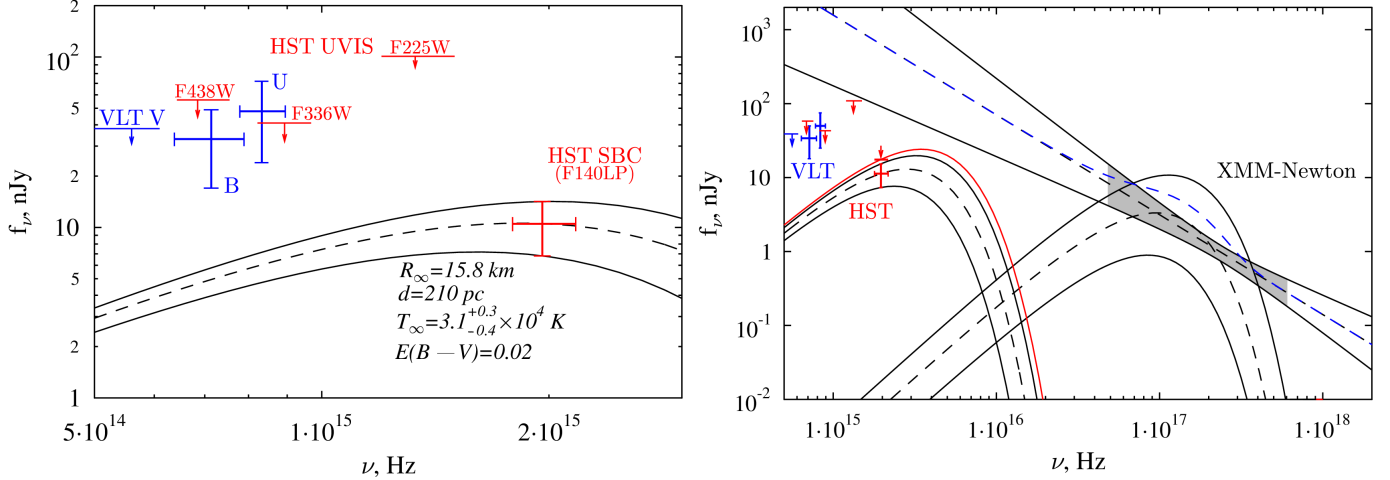


Figure 7. Limits on thermal emission from the NS surface. *Left:* Unabsorbed optical-UV blackbody spectrum assuming the F140LP flux is fully thermal, for $R_\infty = 15.8$ km, $d = 210$ pc, $E(B-V) = 0.02$, and surface temperature $T_\infty = 3.1^{+0.3}_{-0.4} \times 10^4$ K (the temperature uncertainties correspond to the flux uncertainties). *Right:* Dereddened optical-UV thermal spectra extrapolated towards higher energies, and the PL+BB fit to the *XMM-Newton* data (the same as shown in Figure 6). The blackbody spectrum from the entire NS surface shown by black lines is plotted for $d = 300$ pc, $R_\infty = 13.1$ km, $E(B-V) = 0.03$, $T_\infty = 4.8^{+0.7}_{-0.8} \times 10^4$ K. The red line corresponds to a conservative upper limit of the NS surface temperature, $T_\infty < 5.9 \times 10^4$ K, when we consider the F140LP data point as an upper limit, for the same d , R_∞ and $E(B-V)$.

km at $M = 1.4M_\odot$ (Lattimer & Prakash 2016) for the upper bound of the color index, $E(B-V) = 0.03$; these parameters, correspond to a higher temperature, $T_\infty = 4.8^{+0.7}_{-0.8} \times 10^4$ K ($T = 6.3^{+0.8}_{-1.1} \times 10^4$ K). The spectrum is extrapolated towards X-rays, where the unabsorbed PL+BB fit of the *XMM-Newton* spectrum of the pulsar is also shown. We see that emission from the NS surface with such a temperature would not be detectable in the optical and X-rays. If we assume that the F140LP detection was not real, then the 3σ upper bound on the FUV flux density, $f_{\text{F140LP}} < 14$ nJy, gives us an upper limit on the temperature – e.g., $T_\infty < 5.9 \times 10^4$ K ($T < 7.7 \times 10^4$ K) at $d = 300$ pc, $R_\infty = 13.1$ km, $E(B-V) = 0.03$ (the corresponding thermal spectrum is shown by the red line in the right panel of Figure 7).

It is interesting to compare the obtained constraints on the surface temperature of the 196 Myr old PSR J0108–1431 with those for other old pulsars. Based on the upper limit, $T_\infty \lesssim 6 \times 10^4$ K, we can conclude that PSR J0108–1431 is colder than the 17 Myr old PSR B0950+08, the only old ordinary pulsar whose thermal emission has been detected, with T_∞ in the range of $(1-3) \times 10^5$ K (Pavlov et al. 2017).

If the F140LP detection of thermal emission from PSR J0108–1431 was real, then the plausible temperature range, $T_\infty \approx (2.7-5.5) \times 10^4$ K, is just slightly above the conservative upper limit, $T_\infty \lesssim 3.2 \times 10^4$ K, for

the 330 Myr old PSR J2144–3933 (Guillot et al. 2019)⁸. The highest temperature of this range is lower than the surface temperature, $T_\infty \approx (1.2 - 3.5) \times 10^5$ K, of the 7 Gyr old nearest millisecond (recycled) pulsar (MSP) J0437–4715 (Kargaltsev et al. 2004; Durant et al. 2012; González-Caniulef et al. 2019). It means that either thermal evolution of NSs is not monotonous or it proceeded differently for J0108–1431 and J0437–4715, e.g., because old ordinary and recycled pulsars have some different properties, including periods and their derivatives, magnetic field strengths and masses (González-Jiménez et al. 2015).

Confirmation of the possible detection of thermal emission from J0108–1431 would mean that it is the coldest NS whose thermal emission has been detected, but its temperature is still high enough to support the idea that NSs do not just cool passively but some heating mechanisms strongly affect their thermal evolution. According to passive cooling scenarios, cooling of isolated NSs becomes exponentially fast at ages of a few Myr after which thermal emission from their surfaces becomes undetectable (e.g., Yakovlev & Pethick 2004). However, this rapid cooling can be partly compensated by a number of heating mechanisms. One of them is the so-called rotochemical heating due to composition changes (such as the neutron beta decay) forced by density increase

⁸ Guillot et al. (2019) present the upper limit $T \approx 4.2 \times 10^4$ K for unredshifted temperature assuming an NS with $R = 10$ km and $M = 1.4M_\odot$.

as the centrifugal force decreases in the course of NS spindown (Reisenegger 1995; Fernández & Reisenegger 2005). This heating mechanism has a minor effect on surface temperatures of young NSs but its contribution can dominate at ages $\gtrsim 10$ Myr. Another important mechanism is “frictional heating” caused by interaction of vortex lines of the faster rotating neutron superfluid with the slower rotating normal matter in the inner NS crust (Alpar et al. 1984; Larson & Link 1999).

According to the top panel of Figure 5 of Guillot et al. (2019), the upper bound on the (unredshifted) surface temperature of PSR J0108–1431, $T < 8 \times 10^4$ K, is consistent with the values predicted by the models of rotochemical heating by Gonzalez & Reisenegger (2010) for a 200 Myr old pulsar with the surface magnetic field of 2.4×10^{11} G and initial period at birth of 1 ms, assuming either modified Urca reactions or direct Urca reactions with additional frictional heating with excess angular momentum $J = 1 \times 10^{44}$ erg s (the predicted temperatures are very close to each other at these parameters). This is similar to the younger PSR B0950+08. However, if the FUV thermal emission was actually detected, then the observed temperature range $T \sim (3-7) \times 10^4$ K lies between these predictions and the low temperature boundary provided by the direct Urca models without frictional heating. This would mean that frictional heating is less efficient in PSR J0108–1431 than in PSR B0950+08. To obtain tighter constraints on heating mechanisms, one should re-observe PSR J0108–1431 with deeper exposures as well as observe more old pulsars in the optical-UV.

6. CONCLUSIONS

We observed the field of the nearby 196 Myr old PSR J0108–1431 with the *HST* in four optical-UV bands. We detected a point-like FUV source in the F140LP band at about 3σ significance level with coordinates coinciding with the position of the pulsar within the 1σ uncertainty of $0''.2$. We consider this source as a possible FUV counterpart of PSR J0108–1431. Also, we placed upper limits on the flux densities of the pulsar in the F225W, F336W and F438W bands. Using more accurate astrometry, we confirmed the 3σ detection of the optical source at the pulsar position in year 2000 in the VLT $U+B$ filters, and its upper limit in the V filter, reported earlier by Mignani et al. (2008).

Assuming that the possibly detected F140LP, U and B emission comes from the pulsar counterpart, we analyzed its multi-wavelength spectral energy distribution, including the archival X-ray data obtained with *XMM-Newton*. We found that the spectral flux density distribution can be described by a power-law model in the optical-UV part, suggesting its magnetospheric origin. The spectrum becomes steeper in X-rays, implying a spectral break between the UV and X-ray ranges. Such behavior is typical for pulsars observed in both ranges. The pulsar has a record high efficiency, $\eta \sim 10^{-2}$, of transformation of the spindown power to nonthermal (magnetospheric) radiation in the optical-UV through X-rays.

In the FUV band, the pulsar emission might be dominated by thermal emission from the bulk of the NS surface. If this is the case, the NS surface temperature is in the range of $(3-6) \times 10^4$ K, as seen by a distant observer – the lowest NS temperature ever measured. At the same time, it is much higher than predicted by scenarios of passive NS cooling at this NS age, which could be due to heating mechanisms operating in the NS interiors. A conservative consideration of the FUV data point as an upper bound yields the 3σ upper limit on the NS brightness temperature, $T_\infty < 6 \times 10^4$ K.

Detection of PSR J0108–1431 in the optical and UV bands at higher significance levels is needed to confirm the counterpart and study its properties.

We thank the referee for useful comments. Support for *HST* program #14249 was provided by NASA through a grant from the Space Telescope Science Institute, which is operated by the Association of Universities for Research in Astronomy, Inc., under NASA contract NAS 5-26555. We thank Bettina Posselt for providing the reduced *XMM-Newton* data. RPM is grateful to Denise Taylor (STScI) for support during the *HST* observations.

Facilities: *HST*/WFC3; *HST*/ACS; VLT/FORS; *XMM-Newton*; *Gaia*

Software: This research made use of the following softwares and packages: IRAF (Tody 1986, 1993), XSPEC (Arnaud 1996), EsoRex (ESO CPL Development Team 2015), Mr-Moose (Drouart & Falkendal 2018)

REFERENCES

- Alpar, M. A., Pines, D., Anderson, P. W., & Shaham, J. 1984, *ApJ*, 276, 325
- Arnaud, K. A. 1996, in *Astronomical Society of the Pacific Conference Series*, Vol. 101, *Astronomical Data Analysis Software and Systems V*, ed. G. H. Jacoby & J. Barnes, 17

- Arumugasamy, P., & Mitra, D. 2019, *MNRAS*, 489, 4589
- Avila, R. J., Bohlin, R., Hathi, N., et al. 2019, *SBC Absolute Flux Calibration*, Tech. rep.
- Avila, R. J., & Chiaberge, M. 2016, *Photometric Aperture Corrections for the ACS/SBC*, Tech. rep.
- Cardelli, J. A., Clayton, G. C., & Mathis, J. S. 1989, *ApJ*, 345, 245
- Deller, A. T., Tingay, S. J., Bailes, M., & Reynolds, J. E. 2009, *ApJ*, 701, 1243
- Drouart, G., & Falkendal, T. 2018, *MNRAS*, 477, 4981
- Durant, M., Kargaltsev, O., Pavlov, G. G., et al. 2012, *ApJ*, 746, 6
- ESO CPL Development Team. 2015, *EsoRex: ESO Recipe Execution Tool*, , ascl:1504.003
- Fernández, R., & Reisenegger, A. 2005, *ApJ*, 625, 291
- Gonzalez, D., & Reisenegger, A. 2010, *A&A*, 522, A16
- González-Caniulef, D., Guillot, S., & Reisenegger, A. 2019, *MNRAS*, 490, 5848
- González-Jiménez, N., Petrovich, C., & Reisenegger, A. 2015, *MNRAS*, 447, 2073
- Green, G. M., Schlafly, E. F., Finkbeiner, D., et al. 2018, *MNRAS*, 478, 651
- Guillot, S., Pavlov, G. G., Reyes, C., et al. 2019, *ApJ*, 874, 175
- He, C., Ng, C. Y., & Kaspi, V. M. 2013, *ApJ*, 768, 64
- Kargaltsev, O., & Pavlov, G. 2007, *Ap&SS*, 308, 287
- Kargaltsev, O., Pavlov, G. G., & Romani, R. W. 2004, *ApJ*, 602, 327
- Kashyap, V. L., van Dyk, D. A., Connors, A., et al. 2010, *ApJ*, 719, 900
- Kirichenko, A., Danilenko, A., Shternin, P., et al. 2015, *ApJ*, 802, 17
- Koptsevich, A. B., Pavlov, G. G., Zharikov, S. V., et al. 2001, *A&A*, 370, 1004
- Kozhurina-Platais, V., & Anderson, J. 2015, *Standard Astrometric Catalog and Stability of WFC3/UVIS Geometric Distortion*, *Space Telescope WFC Instrument Science Report 2015-02*
- Larson, M. B., & Link, B. 1999, *ApJ*, 521, 271
- Lattimer, J. M., & Prakash, M. 2016, *PhR*, 621, 127
- Lindgren, L., Hernández, J., Bombrun, A., et al. 2018, *A&A*, 616, A2
- Manchester, R. N., Lyne, A. G., D'Amico, N., et al. 1996, *MNRAS*, 279, 1235
- Mignani, R. P. 2011, *Advances in Space Research*, 47, 1281
- Mignani, R. P., De Luca, A., Caraveo, P. A., & Becker, W. 2002, *ApJL*, 580, L147
- Mignani, R. P., Manchester, R. N., & Pavlov, G. G. 2003, *ApJ*, 582, 978
- Mignani, R. P., Pavlov, G. G., & Kargaltsev, O. 2008, *A&A*, 488, 1027
- . 2010, *ApJ*, 720, 1635
- . 2011, *A&A*, 531, A105
- Mignani, R. P., Shearer, A., de Luca, A., et al. 2019, *ApJ*, 871, 246
- Neuschaefer, L. W., & Windhorst, R. A. 1995, *ApJS*, 96, 371
- Pavlov, G. G., Kargaltsev, O., Wong, J. A., & Garmire, G. P. 2009, *ApJ*, 691, 458
- Pavlov, G. G., Rangelov, B., Kargaltsev, O., et al. 2017, *ApJ*, 850, 79
- Pavlov, G. G., Stringfellow, G. S., & Cordova, F. A. 1996, *ApJ*, 467, 370
- Posselt, B., Arumugasamy, P., Pavlov, G. G., et al. 2012, *ApJ*, 761, 117
- Posselt, B., Popov, S. B., Haberl, F., et al. 2007, *Ap&SS*, 308, 171
- . 2008, *A&A*, 482, 617
- Rangelov, B., Pavlov, G. G., Kargaltsev, O., et al. 2017, *ApJ*, 835, 264
- Reisenegger, A. 1995, *ApJ*, 442, 749
- Sawicki, M. 2012, *PASP*, 124, 1208
- Shibanov, Y. A., Zharikov, S. V., Komarova, V. N., et al. 2006, *A&A*, 448, 313
- Sznajder, M., & Geppert, U. 2020, *MNRAS*, 493, 3770
- Tauris, T. M., Nicastro, L., Johnston, S., et al. 1994, *ApJL*, 428, L53
- Tody, D. 1986, in *Society of Photo-Optical Instrumentation Engineers (SPIE) Conference Series*, Vol. 627, *Instrumentation in astronomy VI*, ed. D. L. Crawford, 733
- Tody, D. 1993, in *Astronomical Society of the Pacific Conference Series*, Vol. 52, *Astronomical Data Analysis Software and Systems II*, ed. R. J. Hanisch, R. J. V. Brissenden, & J. Barnes, 173
- Verbiest, J. P. W., Weisberg, J. M., Chael, A. A., Lee, K. J., & Lorimer, D. R. 2012, *ApJ*, 755, 39
- Watson, D. 2011, *A&A*, 533, A16
- Yakovlev, D. G., & Pethick, C. J. 2004, *ARA&A*, 42, 169
- Zavlin, V. E., & Pavlov, G. G. 2004, *ApJ*, 616, 452
- Zharikov, S., & Mignani, R. P. 2013, *MNRAS*, 435, 2227
- Zharikov, S., Shibanov, Y., & Komarova, V. 2006, *Advances in Space Research*, 37, 1979
- Zharikov, S. V., Shibanov, Y. A., Mennickent, R. E., & Komarova, V. N. 2008, *A&A*, 479, 793
- Zharikov, S. V., Shibanov, Y. A., Mennickent, R. E., et al. 2004, *A&A*, 417, 1017
- Zharikov, S. V., Shibanov, Y. A., Koptsevich, A. B., et al. 2002, *A&A*, 394, 633